Wide Linearity Range 3D Magnetic Sensor and Angular Position Detector Based on a Single FePt Spin−Orbit Torque Device

Ying Tao, Zhe Guo, Shihao Li, Liu Yang, Fang Jin, Long You,* Rujun Tang, and Kaifeng Dong*

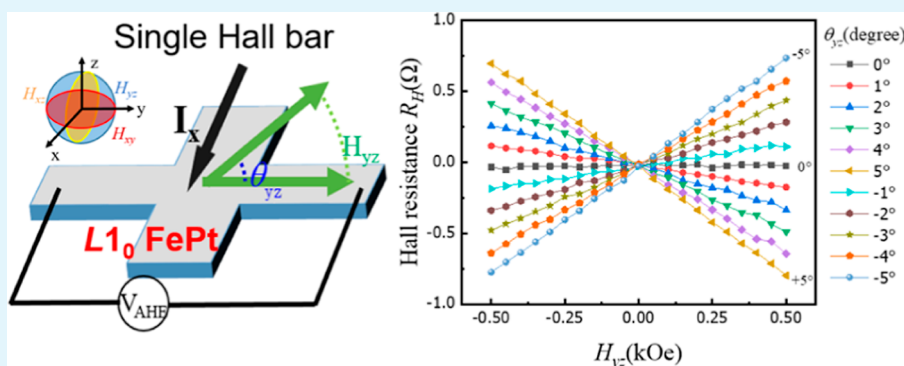Cite This: *ACS Appl. Mater. Interfaces* 2024, 16, 27917−27925

Read Online

ACCESS | Metrics & More | Article Recommendations | Supporting Information

ABSTRACT: Three-dimensional (3D) vector magnetic sensors play a significant role in a variety of industries, especially in the automotive industry, which enables the control of precise position, angle, and rotation of motion elements. Traditional 3D magnetic sensors integrate multiple sensors with their sensing orientations along the three coordinate axes, leading to a large size and inevitable nonorthogonal misalignment. Here, we demonstrate a wide linearity range 3D magnetic sensor utilizing a single $L1_0$-FePt Hall-bar device, whose sensitivity is 291 VA^{-1} T^{-1} in the z-axis and 27 VA^{-1} T^{-1} in the in-plane axis. Based on the spin−orbit torque-dominated magnetization reversal, the linear response of anomalous Hall resistance within a large linear range (±200 Oe) for the x, y, and z components of magnetic fields has been obtained, respectively. Typically, it exhibits a relatively lower magnetic noise level of 7.9 nV at 1 Hz than previous results, improving measurement resolution at the low frequency. Furthermore, we provide a straightforward approach for noncontact angular position detection based on a single Hall-bar device, which shows great potential for application in rotational motion control.

KEYWORDS: $L1_0$ FePt, perpendicular magnetic anisotropy, spin−orbit torque, 3D magnetic sensor, angular position detection

1. INTRODUCTION

A variety of magnetic sensors[1] have been widely employed in geomagnetic navigation,[2] biomagnetic sensing,[3] and the automotive industry.[4,5] Especially, the demand for magnetoresistive sensors, including anisotropic magnetoresistance[6] (AMR), giant magnetoresistance[7] (GMR), and tunnel magnetoresistance[8] (TMR) sensors, is increasing dramatically due to their low cost, robust endurance, and high reliability in the automotive industry.[9−11] Besides, the superconducting quantum interference device (SQUID) is the most sensitive technology for some ultrasensitive electronic and magnetic measurements.[12] However, most of the commonly used magnetic sensors create an output electrical signal that is proportional to the scalar quantity of the magnetic field along a principal axis. To detect the field components in three orthogonal directions directly, the traditional approach is to integrate multiple sensitive devices with their sensitive directions along the three coordinate axes.[13,14] This not only necessitates three power sources but also leads to a

complicated microelectronic design, a large sensor size, low spatial resolution, and inevitable nonorthogonal misalignment.[15] Thus, the development of 3D vector magnetic sensors based on a single planar-type device with low power consumption and a simple measurement unit is necessary.[16]

Recently, intriguing physical phenomena such as spin−orbit torque (SOT) and the anomalous Hall effect (AHE) are promising to motivate the development of a planar 3D magnetic sensor beyond traditional Hall and MR devices.[17] Based on the SOT effect, Wu et al. proposed the spin torque gate (STG) magnetic field sensor, which can achieve a linear response to magnetic field without any magnetic bias, in a
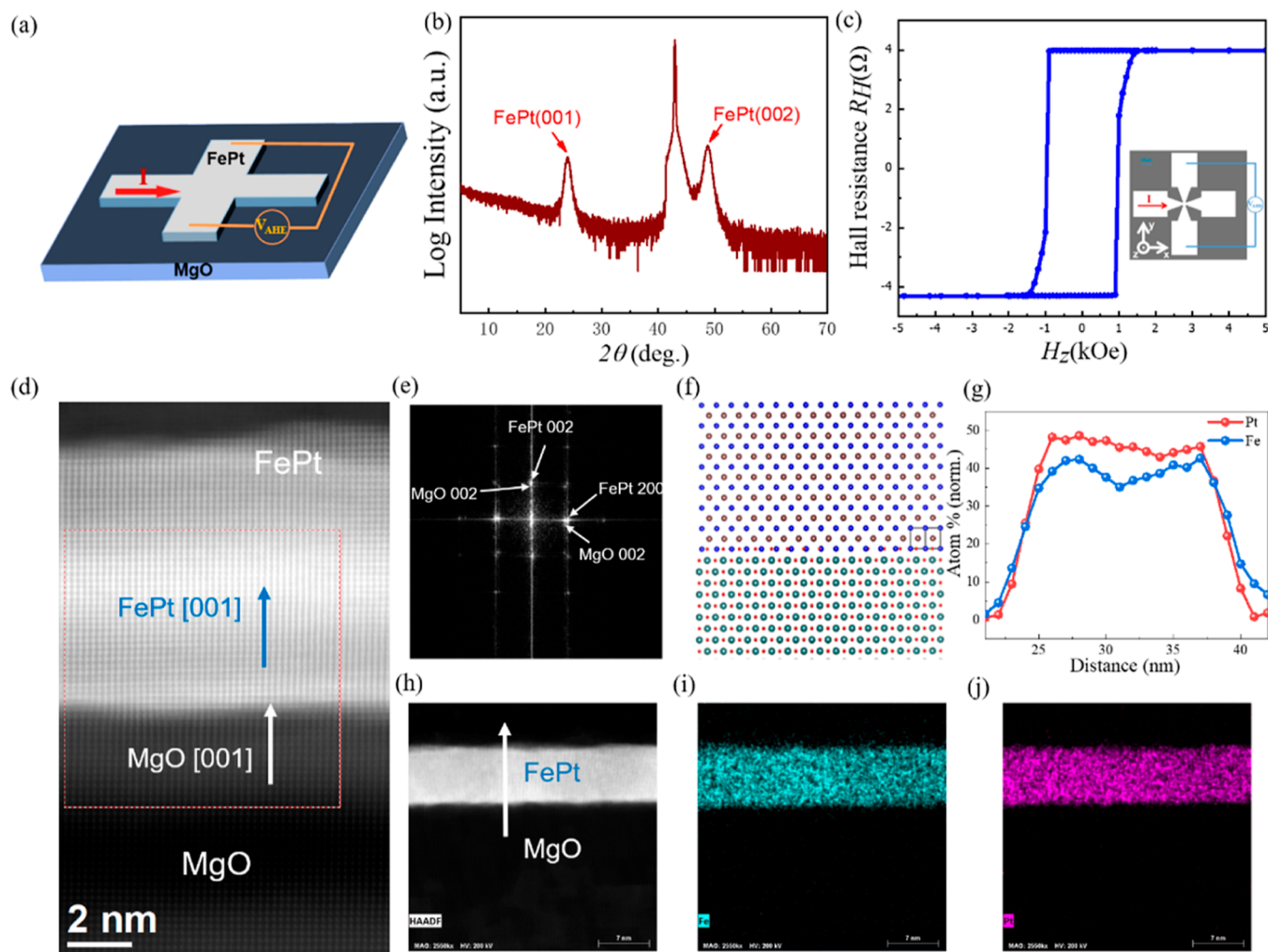
Figure 1. (a) Hall-bar device structure. (b) XRD spectra of the 6 nm $L1_0$-FePt sample. (c) AHE loops of the device with high PMA. (d−j) $L1_0$-FePt crystal structure and TEM picture of FePt. (i,j) Energy dispersive X-ray (EDX) elemental mapping of Fe and Pt, respectively.

simple Hall bar structure.[18] Additionally, You et al. have put forward an ingenious approach to distinguishing the three magnetic field components (H_x, H_y, and H_z) with alternating driving current directions in a single Hall-bar device.[19,20] Moreover, Liu et al. demonstrated the ultrahigh sensitivity and low current density in the SOT device with easy-cone magnetic state by exquisite engineering of the magnetic anisotropy in the Pt/Co/Ta heterostructure.[21] However, the linear range of the above 3D sensors is relatively small, only tens of Oe for the in-plane (IP) and out-of-plane (OP) magnetic field components. For applications such as current sensing[22] and automotive systems[4] (antilock braking systems, camshafts, crankshafts, pedal positions, transmission speeds, etc.), some properties, including a large linear sensing regime, relaxed design requirements for the field-generating components (such as permanent magnets), negligible magnetic hysteresis, and low-frequency noise, are required.

Here, we demonstrate a wide linearity range 3D magnetic sensor utilizing a single $L1_0$-FePt Hall-bar device with large coercivity. Based on the SOT-dominated magnetization reversal, the linear response of anomalous Hall resistance within a wide linear range (± 200 Oe) for the x, y, and z components of magnetic fields has been obtained, respectively. More importantly, compared to the previous studies by Li et al. (1450 nV $Hz^{-1/2}$)[18] and Guo et al. (411 nV $Hz^{-1/2}$),[20] our

sensor exhibits a relatively lower magnetic noise level of 7.9 nV $Hz^{-1/2}$, improving measurement resolution at the low frequency. The high perpendicular magnetic anisotropy (PMA) of $L1_0$-FePt is able to reduce the sensitivity to temperature variations and external magnetic fields, ensuring reliable long-term performance. Furthermore, we provide a straightforward scheme for noncontact magnetic angular position detection based on a single Hall-bar device, which shows great potential for application in rotational motion control.

2. EXPERIMENTAL SECTION

Utilizing high-temperature deposition at 500 °C, followed by annealing to room temperature within the primary sputtering chamber, we obtained the epitaxial growth of 6 nm $L1_0$-ordered FePt films on the (001) MgO single-crystal substrate. This was accomplished through DC sputtering of the $Fe_{55}Pt_{45}$ target under an argon pressure of 3 mTorr and 50 W power. The magnetron sputtering system maintained a base vacuum pressure smaller than 5 × 10^{-8} Torr. Subsequently, the sample underwent patterning into a Hall bar structure using photolithography and ion milling techniques. The line widths for the current in the x and y channels are both 15 μm, as shown in Figure 1a. Utilizing electron-beam lithography (EBL), we fabricated submicron Hall-bar devices with current line widths of 500 and 800 nm, respectively (Section S1, Supporting Information). X-ray diffraction (XRD) is employed to characterize the
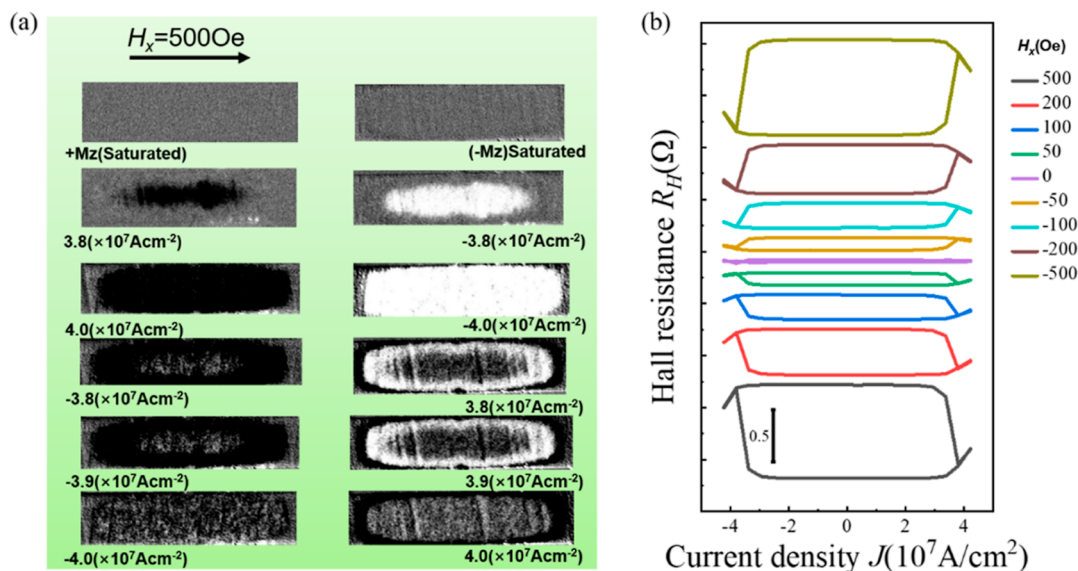
Figure 2. (a) MOKE images of SOT-driven domain wall nucleation and motion. (b) Current-induced magnetization switching with different external fields H_x.
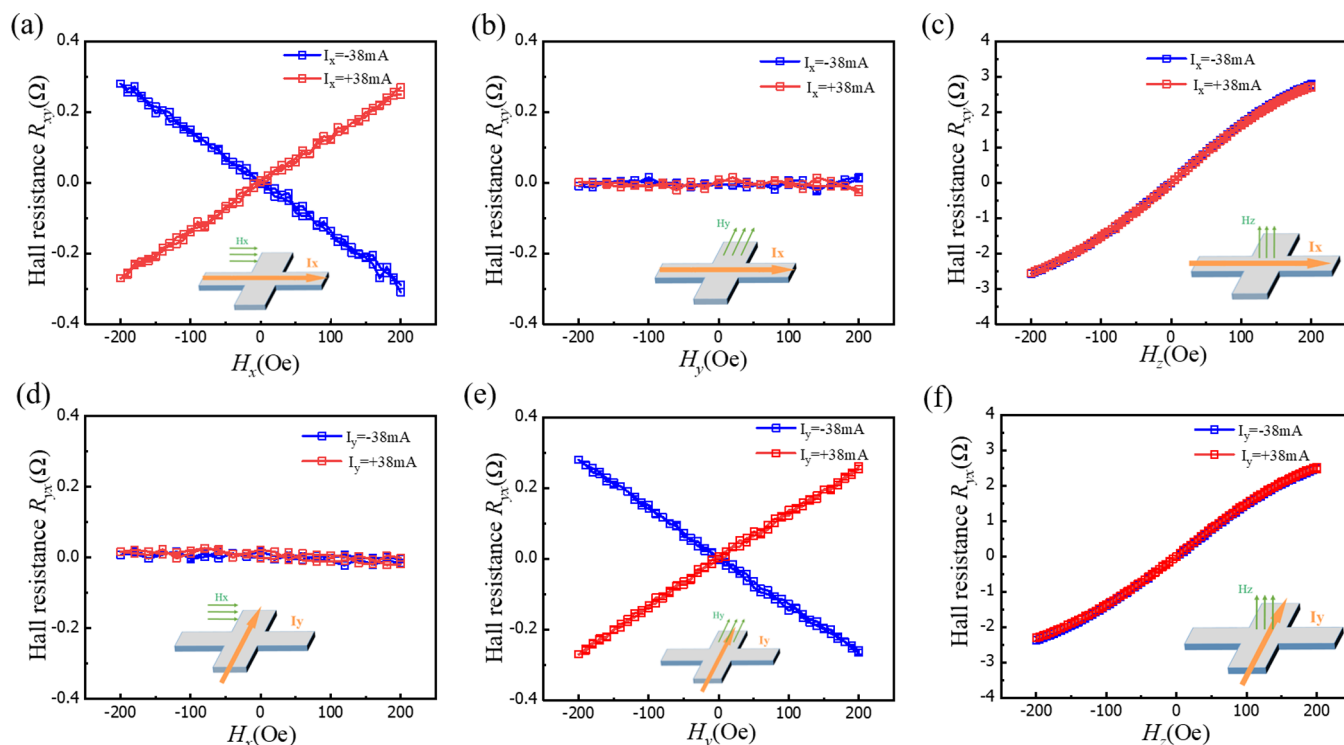

Figure 3. R_{xy} as a function of (a) H_x, (b) H_y, and (c) H_z when I_x = +38 (red curves) and −38 mA (blue curves). Magnetic fields are scanned forward and backward between +200 and −200 Oe in each direction. R_{yx} as a function of (d) H_x, (e) H_y, and (f) H_z under I_y = +38 (red curves) and −38 mA (blue curves).

crystal structure of the films, while transmission electron microscopy (TEM) is used to analyze the microstructure of the films. For the electrical measurements, we applied DC currents with a precision current source (Keithley 6221) and measured the Hall voltage with a nanovoltmeter (Keithley 2182A). We measure the anomalous Hall resistance R_H, which is proportional to the average vertical component of the FePt magnetization M_z. For the DW motion observations stated in the main article, a pulse current with a duration of 1 ms was utilized. The anomalous Hall resistance was measured using a continuous reading current of 0.1 mA. The magnetization reversal process was visualized using magneto-optical Kerr effect (MOKE)

microscopy to elucidate the magnetization switching mode. To perform noise measurements, we used an SR780 FFT network signal analyzer (Stanford) to measure the low frequency noise characterization of our device, and we applied the read current continuously until the noise spectrum was scanned during each measurement. All measurements were performed at room temperature.

3. RESULTS AND DISCUSSION

The XRD spectra of the FePt film sample are shown in Figure 1b. FePt (001) and FePt (002) peaks are observed in Figure 1b, indicating a good $L1_0$ structure for FePt films. Moreover,
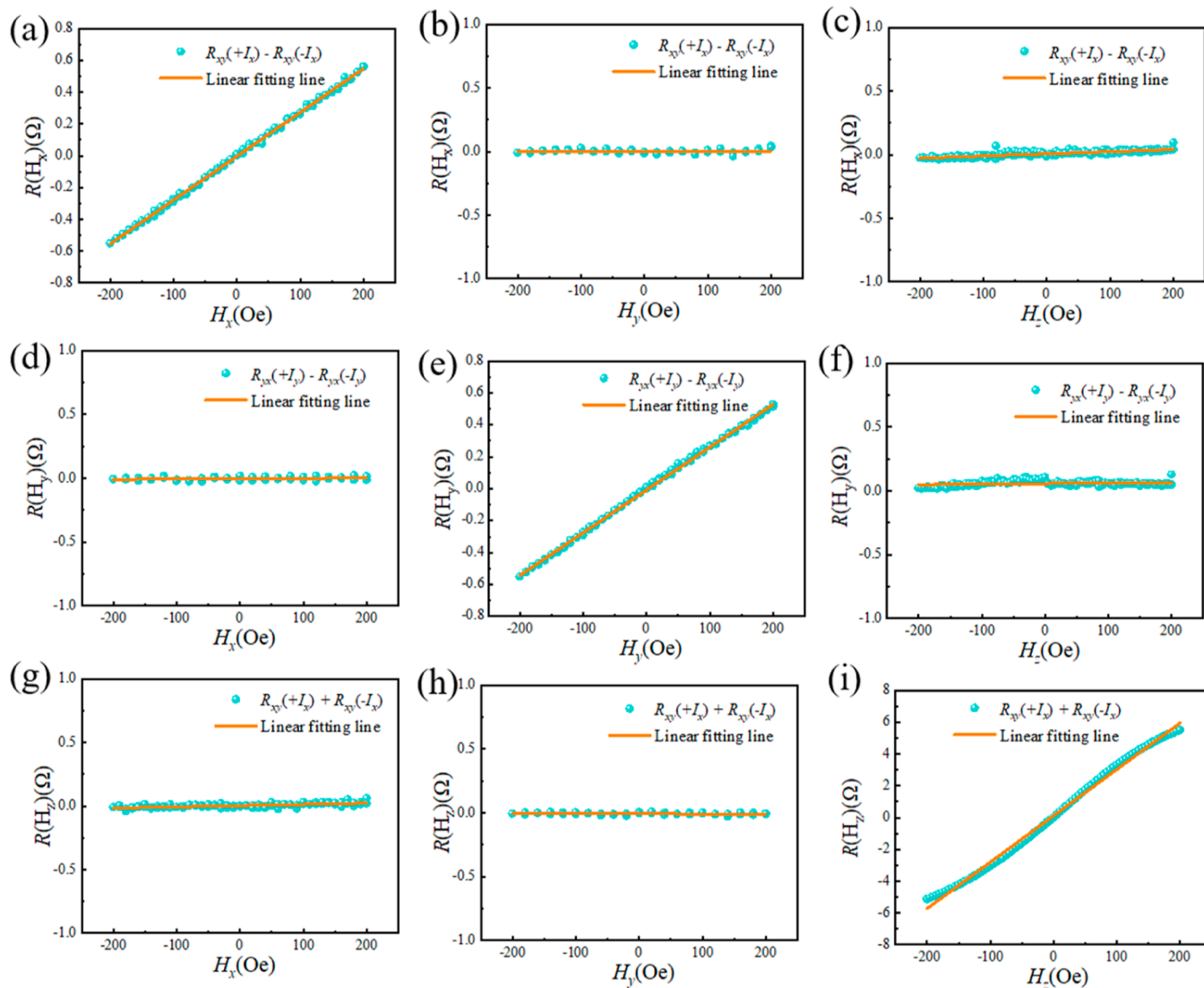
Figure 4. Net resistance $R(H_x)$ as a function of (a) H_x, (b) H_y, and (c) H_z, in that order. Linear fitting line is represented by the orange straight line. Equivalent situations for the net resistances of (d)−(f) $R(H_y)$ and (g)−(i) $R(H_z)$, respectively.

Figure 1c illustrates the anomalous Hall resistance R_H as a function of H_z with a small reading current (0.1 mA), indicating that the FePt sample possesses excellent PMA. Furthermore, high-resolution cross-sectional scanning transmission electron microscopy (STEM) and energy-dispersive X-ray spectroscopy (EDS) were employed to obtain the high-quality phase maps of FePt film. Highly ordered alternately stacked Fe and Pt atomic layers can be seen in the high-resolution high-angle annular dark field (HAADF) image in Figure 1h. Remarkably, both the Pt and Fe compositions display spatial variations, as shown in Figure 1g. The EDS mappings in Figure 1i,j illustrate the corresponding element distributions of both Fe and Pt.

Current-induced magnetization switching was under the external IP magnetic field, while pulsed currents (pulse duration of 500 us) with varying amplitude were applied to the 15 μm line-width Hall-bar device. By using polar MOKE microscopy, as seen in Figure 2a, the switching process was simultaneously captured and observed. As the bright and dark contrasts in the Kerr pictures scale with the up and down magnetization components, respectively, the sequential changes in Kerr contrast exhibited in Figure 2b demonstrate

perpendicular magnetization switching in the Hall-bar device. It is noted that there exists a partial switching behavior by comparing the switching loop in Figure 2b with the anomalous Hall loop in Figure 1c, which is similar to the previous results.[23,24] The switching ratio increases with increasing the external magnetic field H_x and the maximal switching ratio is around 10%. Moreover, the switching direction reverses with the direction of the magnetic field, as shown in Figure 2b. The role of the SOT effect can be equivalent to an OP effective field, the magnitude of which is given by[25]

$$H_z^{SOT} = \frac{\hbar}{2eM_s t}\theta_{SH}J_{x(y)}m_{x(y)} \tag{1}$$

where t is the thickness of ferromagnetic layer, h is the reduced Planck's constant, e is the electron charge, M_s is the saturation magnetization, θ_{SH} is the spin Hall angle, and J is the current density.

Based on the opposite responses to the contrary pulse polarities, we consider the sensing of a vector magnetic field. Then, we first investigated $R_{xy}(R_{yx})$ as a function of H_x and H_y under $I_x(I_y) = \pm 38$ mA. As shown in Figure 3a,d, both $R_{xy}−H_x$
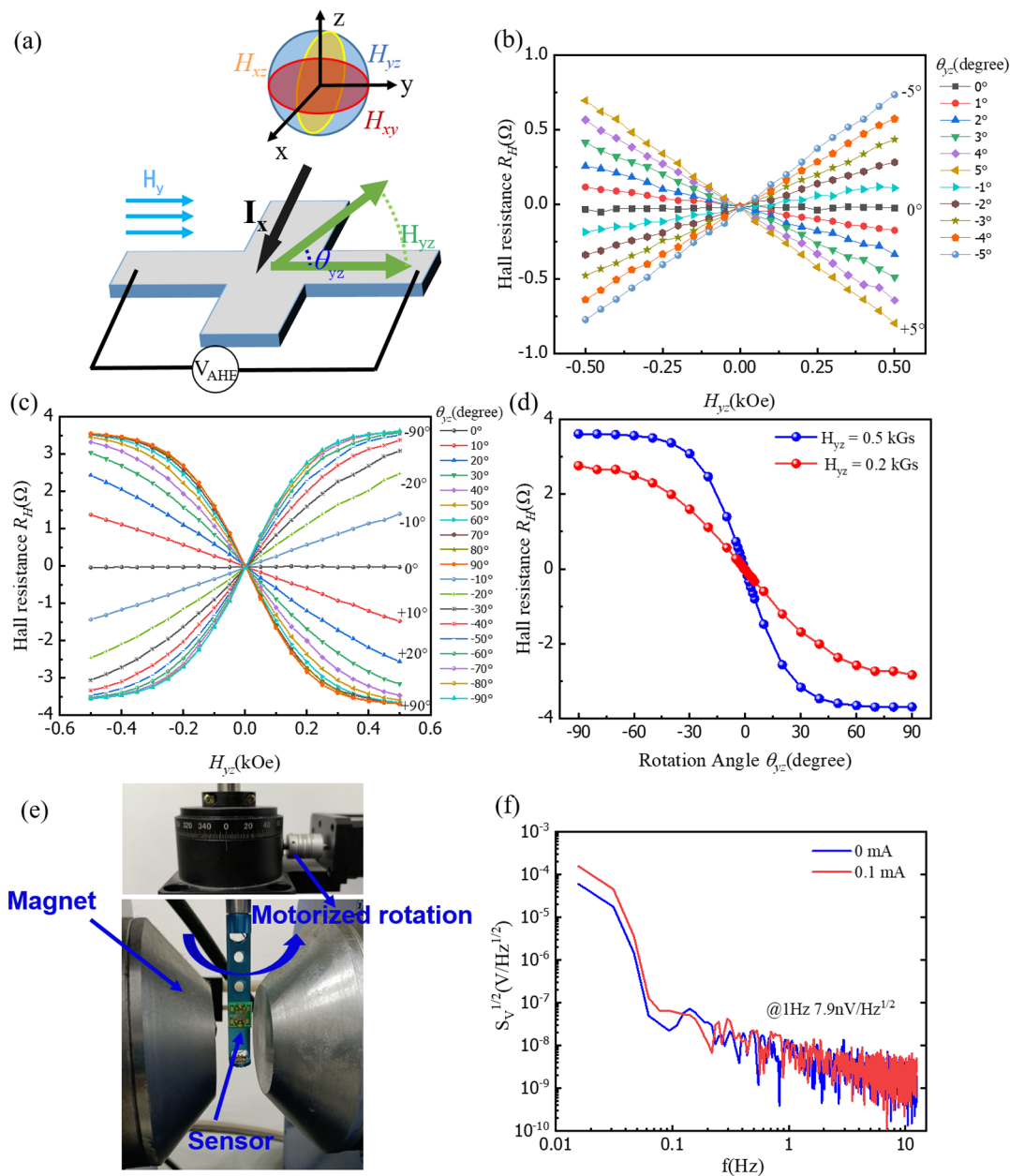
Figure 5. (a) Current and magnetic setup in the angular rotation measurement. (b) R_H as a function of H_{yz} with different angles θ_{yz} from +5 to −5°. (c) R_H as a function of H_{yz} with different angles θ_{yz} from +90 to −90°. (d) θ_{yz} as a function of R_H. (e) Experimental setup for the angular rotation measurement. (f) Noise spectrum of the sensor device, measured at a reading current of 0.1 mA, plotted as $S_V^{1/2}$ versus frequency.

and R_{yx}–H_y curves are symmetrical with respect to the horizontal coordinate, which can be attributed to the different polarities of SOT. As indicated in eq 1, the direction of the SOT effective field is determined by both the current direction and the IP magnetic field. For example, the current $I_x(I_y)$ = +38 mA generates a positive SOT effective field and promotes driving grain switching from downward to upward, resulting in positive $R_{xy}(R_{yx})$ under positive $H_x(H_y)$. In contrast, when $I_x(I_y)$ = −38 mA, the opposite variations of $R_{xy}(R_{yx})$ are obtained. Meanwhile, from Figure 3a,d, it can be seen that R_{xy} and R_{yx} fluctuate linearly with H_x and H_y, respectively, within the range of −200 to +200 Oe. In contrary, the AHE resistance remains constant when the applied current is directed perpendicular to the magnetic field, as shown in Figure 3b,c. On the other hand, because the H_z-induced grain reversal is independent of the IP current direction, the variation

correlations between $R_{xy}(R_{yx})$ and H_z are the same regardless of whether $I_x(I_y)$ is positive or negative [Figure 3d,f].

In order to sense the 3D magnetic field, which may be divided into three mutually orthogonal magnetic field components (H_x, H_y, and H_z), we can take advantage of the differing responses of $R_{xy}(R_{yx})$ to IP and OP fields under positive and negative IP currents. $R_{xy}(+I_x)$, $R_{xy}(−I_x)$, $R_{yx}(+I_y)$, and $R_{yx}(−I_y)$ represent the AHE resistance values for positive and negative writing currents in the x and y axes, respectively. We can make a subtraction operation between $R_{xy}(+I_x)$ and $R_{xy}(−I_x)$ to remove the contribution from H_z in accordance with the symmetry of R−H curves under various current polarities. The H_y field component makes no contribution to the Hall resistance when I_x is applied, hence eq 2 can be used to get the net resistance contribution from just the H_x component. As our Hall-bar device is designed with equal

Table 1. Performance of Our 3D Magnetic Sensor and Comparison with Other 3D Sensors[a]

characteristics	system structure	dynamic range	resolution	sensitivity	linearity error	noise @1 Hz
SOT/domain nucleation (this work)	one Hall bar (FePt single layer)	±200 Oe (H_x)	2873 nT	27.5 VA^{-1} T^{-1}	2.8%	7.9 nV Hz$^{-1/2}$
	$15 \times 50~\mu m^2$	±200 Oe (H_y)	2959 nT	26.7 VA^{-1} T^{-1}	3.0%	
		±200 Oe (H_z)	271.2 nT	291.2 VA^{-1} T^{-1}	5.1%	
SOT/domain nucleation[20]	one Hall bar (W/CoFeB/MgO)	±20 Oe (H_x)	1090 nT	377 VA^{-1} T^{-1}	2.3%	411 nV Hz$^{-1/2}$
	$40 \times 200~\mu m^2$	±20 Oe (H_y)	1191 nT	345 VA^{-1} T^{-1}	2.9%	
		±20 Oe (H_z)	657.6 nT	625 VA^{-1} T^{-1}	3.3%	
SOT/domain wall motion[19]	one Hall bar (Ta/CoFeB/MgO)	±10 Oe (H_x)	7073 nT	205 VA^{-1} T^{-1}	3.2%	1450 nV Hz$^{-1/2}$
	$50 \times 200~\mu m^2$	±10 Oe (H_y)	5142 nT	282 VA^{-1} T^{-1}	2.7%	
		±4 Oe (H_z)	786 nT	1845 VA^{-1} T^{-1}	4.3%	
AHE/SOT[21]	one Hall bar (Co/Pt bilayer)	±30 Oe (H_x)	3386 nT	410 VA^{-1} T^{-1}	3.2%	3386 nT Hz$^{-1/2}$
	$50 \times 250~\mu m^2$	±25 Oe (H_y)	2869 nT	484 VA^{-1} T^{-1}	2.9%	2869 nT Hz$^{-1/2}$
		±1 Oe (H_z)	88 nT	15,778 VA^{-1} T^{-1}	1.9%	88 nT Hz$^{-1/2}$
SOT/easy-cone magnetic state with 2 AMR sensors[21]	AHE + 2 AMR sensors (planar)	±1.5 Oe (H_x)	1.44 nT	28.5 VV^{-1} T^{-1}	NA	1.44 nT Hz$^{-1/2}$
		±1.5 Oe (H_y)	1.84 nT	30.5 VV^{-1} T^{-1}		1.84 nT Hz$^{-1/2}$
		±0.5 Oe (H_z)	27.7 nT	31,196 VV^{-1} T^{-1}		27.7 nT Hz$^{-1/2}$
AMR sensor (HMC1023, Honeywell)	3 Wheatstone bridges	±6 Oe (H_x)	8.5 nT	10 VV^{-1} T^{-1}	NA	8.5 nT Hz$^{-1/2}$
		±6 Oe (H_y)	8.5 nT	10 VV^{-1} T^{-1}		8.5 nT Hz$^{-1/2}$
		±6 Oe (H_z)	8.5 nT	10 VV^{-1} T^{-1}		8.5 nT Hz$^{-1/2}$
GMR sensor[27]	fluxguide+ 4 GMR sensors	±3 Oe (H_x)	3−9 nT	575 VV^{-1} T^{-1}	NA	1380 nV Hz$^{-1/2}$
		±3 Oe (H_y)	3−9 nT	600 VV^{-1} T^{-1}		1440 nV Hz$^{-1/2}$
		±3 Oe (H_z)	3−9 nT	550 VV^{-1} T^{-1}		1320 nV Hz$^{-1/2}$
TMR sensor[28] (TMR 2305, MultiDimension Technology)	3 Wheatstone bridges	±10 Oe (H_x)	2 nT	250 VV^{-1} T^{-1}	2%	500 nV Hz$^{-1/2}$
		±10 Oe (H_y)	2 nT	250 VV^{-1} T^{-1}	2%	
		±10 Oe (H_z)	2 nT	250 VV^{-1} T^{-1}	2%	
Fluxgate magnetometer[29]	one fluxgate	±1.5 Oe (H_x)	0.11 nT	122.4 V/T	10%	13.5 nV Hz$^{-1/2}$
	one planar excitation coil	±1.5 Oe (H_y)	0.11 nT	122.4 V/T	10%	13.5 nV Hz$^{-1/2}$
	four planar pick-up coils	±1.5 Oe (H_z)	1.16 nT	11.6 V/T	10%	13.5 nV Hz$^{-1/2}$

[a]NA: not applicable. The linear field range, sensitivity, linearity error, and 1/f noise for all sensor types in 1 are shown in the order for H_x, H_y, and H_z, respectively.

line widths in both the x and y directions, similarly, I H_y contribution can be determined by the subtraction of $R_{yx}(+I_y)$ and $R_{yx}(-I_y)$. Thus, R_{yx} is sensitive to H_y and H_z, but insensitive to H_x, when I_y is applied, which enables the measurement of y-axis component of the magnetic field upon applying a current pulse in the y channel. Moreover, through adding $R_{xy}(+I_x)$ and $R_{xy}(-I_x)$, the contribution of H_x is removed, leaving H_z as the single contributor to the net resistance. We can therefore determine each component of a 3D magnetic field by Hall resistance measurement based on these mathematical operations, which are condensed into eqs 2−4. Here, we made slight modifications to the formula, removing the operation of average of the similar formulas in refs [19] and[20]. The average operation requires the additional division analog circuit, which is detrimental for practical signal processing

$$R(H_x) = R_{xy}(+J_x) - R_{xy}(-J_x) \qquad (2)$$

$$R(H_y) = R_{yx}(+J_y) - R_{yx}(-J_y) \qquad (3)$$

By eliminating both contributions from H_x and H_y, one may also get the net resistance contributed just by the H_z component

$$R(H_z) = R_{yx}(+J_y) + R_{yx}(-J_y) \qquad (4)$$

We obtain the linear relationships between the net resistance $R(H_x)$ and H_x, H_y, and H_z according to eq 2 based on the 1D measurements (Figure 3a,c,e), which are depicted in Figure 4a−c, respectively. $R(H_x)$ is as anticipated sensitive to H_x, with a linearity error of 2.8% in the range of −200 to +200 Oe and insensitive to H_y and H_z. The net resistances $R(H_y)$ and $R(H_z)$ are subsequently determined using eqs 3 and 4 (Figure 4d−f,g−i). Similar to the $R(H_x)$ instance, $R(H_y)$ and $R(H_z)$ solely contain contributions from H_y and H_z, respectively. Therefore, the relationships between the net resistances $[R(H_x), R(H_y),$ and $R(H_z)]$ and associated magnetic field components (H_x, H_y, and H_z) are established. In order to perform 3D magnetic field sensing, the magnitude of the appropriate magnetic field components can be read out in accordance with Figure 4a,e,i once the net resistance components have been acquired using

eqs 2−4. The sensitivity of the x, y, and z directions is 27.5, 26.7, and 291.2 VA^{-1} T^{-1}, respectively. It can be found that the sensitivity IP direction is obviously lower than the OP direction, which can be attributed to the partial SOT switching in the $L1_0$-FePt film. Additionally, we have investigated the sensing performance of submicron-sized Hall devices. Furthermore, we have measured SOT switching in submicron Hall-bar devices with line widths of 500 and 800 nm. These devices exhibit a higher switching ratio of the SOT, reaching a maximum of 60% by comparing the OP magnetic field-switched Hall resistance (ΔR_H) with the IP current-switched Hall resistance (ΔR_I), which implies a greater range of adjustable Hall resistance in the IP direction (Section S2, Supporting Information). However, as the device size decreases from micron to nanometer size, thermal fluctuations can induce energy barriers that facilitate the random switching of magnetic domains and there is an increase in linear error. The detailed results and discussion can be referred to in the Supporting Information. Considering it is a nanowire structure, if we further reduce the device size and create a nanodot structure, the device can be transformed into a single-domain structure. This enables the utilization of the linear response characteristics of the domains' random switching probability to detect magnetic fields.[26]

Furthermore, we measured the Hall resistance R_{xy} as a function of the rotating field angle θ_{yz} based on the 15 μm device. The specification of $x-y-z$ coordinates is shown in Figure 5a, along with the design of a 3D sensor mounted in a vector magnetic field. As shown in Figure 5e, the sensor plane is fixed, and the magnetic field direction is rotated in the yz plane. It is found that the Hall resistance R_H and magnetic field H_{yz} have a good linear relationship when the included angle θ_{yz} is within the range of $\pm5°$, as shown in Figure 5b. As the angle θ_{yz} increases, the R_H–H_{yz} curve becomes nonlinear, as shown in Figure 5c. Then we choose the magnetic field of 0.5 and 0.2 kGs to obtain the relationship between the Hall resistance R_H and magnetic field angle θ_{yz}, as shown in Figure 5d. It is found that the θ_{yz}–R_H curve has a good linear relationship when the included angle θ_{yz} is within the range of $\pm30°$, which could be applied to the angular detection. An average angle error of 0.5° within the range of $\pm30°$, and it might be more sensitive by equipping appropriate amplifiers and filters to enhance the sensor's signal processing capability and immunity to interference. Our design, with its extremely straightforward structure, might result in a low-cost angular position sensor.

In Table 1, the performances of our 3D magnetic field sensor are outlined and contrasted with those of competing 3D magnetic field sensors.

When compared to contemporary 3D magnetic sensors (GMR and fluxgate)[27] and commercial (TMR2305, Multi-Dimension Technology),[28] the dynamic ranges of our sensor, referred to as the SOT sensor here, are 1 to 2 orders of magnitude greater. For the 15 μm device within a magnetic field range of ±200 Oe, the linear errors of the sensor in the x, y, and z directions are 2.8, 3.0, and 5.1% (within ±150 Oe, 3.4%), respectively. These linear errors are related to the size of the device and the stochastic switching process of magnetic domains (Sections S3 and S4, Supporting Information). The linearity of our sensor (15 μm) is close to that of the SOT-based 3D sensors reported before, and superior to that of the fluxgate magnetometer[29] within its detectable range. Furthermore, as demonstrated in Figure 5f, the 1/f noise of our SOT sensor is approximately 7.9 nV Hz$^{-1/2}$, which is obviously

lower than that of the Co/Pt bilayer SOT sensor. The low 1/f noise can be attributed to the stable magnetic domain structure of $L1_0$-FePt, and the large coercive field contributes to combating thermal and field disturbances according to the thermal stability factor $\Delta = M_s H_k V / 2k_b T$. Additionally, the 1/f noise of the device may also be related to intrinsic noise from the current source and thermal noise (Section S6, Supporting Information). Compared with other SOT sensors reported before, the dynamic of the SOT sensor is larger by roughly an order of magnitude along the x and y directions, and even 2 orders of magnitude in the z direction. What is more, some other 3D sensors use three or more magnetic sensing elements integrated for 3D magnetic field sensing and generally suffer from cross-sensitivity among the measurement axes, significantly complicating technology fabrication, impeding high spatial resolution, and obstructing the achievement of the desired miniaturization level. In contrast, our SOT sensor base on the $L1_0$-FePt, which uses only one device, advantageously enables vector magnetometer planarization and miniaturization.

4. CONCLUSIONS

In conclusion, we exhibited a wide linearity range 3D magnetic sensors based on a single Hall-bar device. Due to the large perpendicular magnetic anisotropy of the $L1_0$-FePt film, we have obtained a significantly wider linear range in the x, y, and z directions than the works reported before, allowing for the detection of magnetic fields over a broader range of applications. The FePt-based 3D sensor maintains stability due to the high PMA and stable magnetic properties of the FePt material. It exhibits a relatively lower magnetic noise level of 7.9 nV at 1 Hz than previous results,[19,20] improving measurement resolution at the low frequency. Furthermore, based on a single Hall-bar device, we propose a simple scheme for magnetic angular position sensing, which shows great potential application in rotational motion control. Equipping appropriate amplifiers and filters could enhance the sensor's signal processing capability and immunity to interference, potentially making it more sensitive for more applications.

■ ASSOCIATED CONTENT

ⓈI Supporting Information

The Supporting Information is available free of charge at https://pubs.acs.org/doi/10.1021/acsami.4c02874.

> Fabrication of submicron Hall-bar devices; SOT switching loops of different size devices; three-axis linear responses in different size devices; performance comparison of 3D magnetic sensors with different sizes; noise analysis of magnetic field generating equipment; and intrinsic noise analysis of the current source and the thermal noise of device (PDF)

■ AUTHOR INFORMATION

Corresponding Authors

Long You − School of Integrated Circuits, Huazhong University of Science and Technology, Wuhan 430074, China; ● orcid.org/0000-0001-5713-194X; Email: lyou@hust.edu.cn

Kaifeng Dong − School of Automation, China University of Geosciences, Wuhan 430074, China; Hubei Key Laboratory of Advanced Control and Intelligent Automation for Complex Systems, Wuhan 430074, China; Engineering Research

Center of Intelligent Technology for Geo-Exploration, Ministry of Education, Wuhan 430074, China;
Email: dongkf1981@163.com

Authors

Ying Tao — *School of Automation, China University of Geosciences, Wuhan 430074, China; Hubei Key Laboratory of Advanced Control and Intelligent Automation for Complex Systems, Wuhan 430074, China; Engineering Research Center of Intelligent Technology for Geo-Exploration, Ministry of Education, Wuhan 430074, China;* orcid.org/0000-0001-9017-4896

Zhe Guo — *School of Microelectronics, Hubei University, Wuhan 430062, China*

Shihao Li — *School of Integrated Circuits, Huazhong University of Science and Technology, Wuhan 430074, China*

Liu Yang — *School of Automation, China University of Geosciences, Wuhan 430074, China; Hubei Key Laboratory of Advanced Control and Intelligent Automation for Complex Systems, Wuhan 430074, China; Engineering Research Center of Intelligent Technology for Geo-Exploration, Ministry of Education, Wuhan 430074, China;* orcid.org/0000-0002-3326-4251

Fang Jin — *School of Automation, China University of Geosciences, Wuhan 430074, China; Hubei Key Laboratory of Advanced Control and Intelligent Automation for Complex Systems, Wuhan 430074, China; Engineering Research Center of Intelligent Technology for Geo-Exploration, Ministry of Education, Wuhan 430074, China*

Rujun Tang — *School of Physical Science and Technology, Jiangsu Key Laboratory of Thin Films, Soochow University, Suzhou 215006, China*

Complete contact information is available at:
https://pubs.acs.org/10.1021/acsami.4c02874

Notes

The authors declare no competing financial interest.

■ ACKNOWLEDGMENTS

■ REFERENCES

(1) Freitas, P. P.; Ferreira, R.; Cardoso, S. Spintronic sensors. *Proc. IEEE* **2016**, *104* (10), 1894−1918.

(2) Quintas, J.; Teixeira, F. C.; Pascoal, A.; et al. An Integrated System for Geophysical Navigation of Autonomous Underwater Vehicles. *IFAC-Pap.* **2018**, *51*, 293−298.

(3) Dong, C.; Liang, X.; Gao, J.; Chen, H.; He, Y.; Wei, Y.; Zaeimbashi, M.; Matyushov, A.; Sun, C.; Sun, N. X. Thin film magnetoelectric sensors toward biomagnetism: Materials, devices, and applications. *Adv. Electron. Mater.* **2022**, *8* (6), 2200013.

(4) Suess, D.; Bachleitner-Hofmann, A.; Satz, A.; Weitensfelder, H.; Vogler, C.; Bruckner, F.; Abert, C.; Prügl, K.; Zimmer, J.; Huber, C.; et al. Topologically protected vortex structures for low-noise magnetic sensors with high linear range. *Nat. Electron.* **2018**, *1* (6), 362−370.

(5) Reininger, T.; Welker, F.; von Zeppelin, M.; et al. Sensors in position control applications for industrial automation. *Sens. Actuators A: Phys.* **2006**, *129* (1−2), 270−274.

(6) Wang, Z.; Wang, X.; Li, M.; Gao, Y.; Hu, Z.; Nan, T.; Liang, X.; Chen, H.; Yang, J.; Cash, S.; et al. Highly Sensitive Flexible Magnetic Sensor Based on Anisotropic Magnetoresistance Effect. *Adv. Mater.* **2016**, *28*, 9370−9377.

(7) Wu, K.; Su, D.; Saha, R.; Wang, J. Giant Magnetoresistance (GMR) materials and devices for biomedical and industrial applications. *Spintronics: Materials, Devices and Applications* **2022**, 3−49.

(8) Sun, K.; Qi, P.; Tao, X.; Zhao, W.; Ye, C. Vector Magnetic Field Imaging With High-Resolution TMR Sensor Arrays for Metal Structure Inspection. *IEEE Sens. J.* **2022**, *22* (14), 14513−14521.

(9) Davies, J. E.; Watts, J. D.; Novotny, J.; Huang, D.; Eames, P. G. Magnetoresistive Sensor Detectivity: A Comparative Analysis. *Appl. Phys. Lett.* **2021**, *118* (6), 062401.

(10) Khan, M. A.; Sun, J.; Li, B.; Przybysz, A.; Kosel, J. Magnetic sensors-A review and recent technologies. *Eng. Res. Express* **2021**, *3* (2), 022005.

(11) Lenz, J.; Edelstein, S. Magnetic Sensors and their Applications. *IEEE Sens. J.* **2006**, *6*, 631−649.

(12) Vettoliere, A.; Granata, C. Highly Sensitive Tunable Magnetometer Based on Superconducting Quantum Interference Device. *Sensors* **2023**, *23* (7), 3558.

(13) Wouters, C.; Vranković, V.; Rössler, C.; Sidorov, S.; Ensslin, K.; Wegscheider, W.; Hierold, C. Design and fabrication of an innovative three-axis Hall sensor. *Sens. Actuators A: Phys.* **2016**, *237*, 62−71.

(14) Becker, C.; Karnaushenko, D.; Kang, T.; Karnaushenko, D. D.; Faghih, M.; Mirhajivarzaneh, A.; Schmidt, O. G. Self-assembly of highly sensitive 3D magnetic field vector angular encoders. *Sci. Adv.* **2019**, *5* (12), 7459.

(15) Trinh, X. T.; Jeng, J. T.; Lu, C. C.; Lan, M. J.; Chen, B. C.; Hsu, J. H.; Luong, V. S.; Hsu, H. Y. Miniature tri-axis magnetometer with in-plane GMR sensors. *IEEE Trans. Magn.* **2017**, *53* (11), 1−4.

(16) Shiogai, J.; Fujiwara, K.; Nojima, T.; Tsukazaki, A. Three-Dimensional Sensing of the Magnetic-Field Vector by a Compact Planar-Type Hall Device. *Commun. Mater.* **2021**, *2*, 102.

(17) Chen, X.; Xie, H.; Shen, H.; Wu, Y. Vector Magnetometer Based on a Single Spin-Orbit-Torque Anomalous-Hall Device. *Phys. Rev. Appl.* **2022**, *18* (2), 024010.

(18) Xie, H.; Chen, X.; Luo, Z.; Wu, Y. Spin Torque Gate Magnetic Field Sensor. *Phys. Rev. Appl.* **2021**, *15* (2), 024041.

(19) Li, R.; Zhang, S.; Luo, S.; Guo, Z.; Xu, Y.; Ouyang, J.; Song, M.; Zou, Q.; Xi, L.; Yang, X.; et al. A Spin−Orbit Torque Device for Sensing Three-Dimensional Magnetic Fields. *Nat. Electron.* **2021**, *4*, 179−184.

(20) Guo, Z.; Li, R.; Zhang, S.; Tian, Y.; Hong, J.; You, L. A Three-Dimensional Magnetic Field Sensor Based on a Single Spin−Orbit-Torque Device Via Domain Nucleation. *Appl. Phys. Lett.* **2022**, *120*, 232404.

(21) Su, W.; Hu, Z.; Li, Y.; Han, Y.; Chen, Y.; Wang, C.; Jiang, Z.; He, Z.; Wu, J.; Zhou, Z.; et al. Easy-Cone Magnetic State Induced Ultrahigh Sensitivity and Low Driving Current in Spin-Orbit Coupling 3D Magnetic Sensors. *Adv. Funct. Mater.* **2022**, *33*, 2211752.

(22) Tsukada, K.; Hayashi, M.; Nakamura, Y.; Sakai, K.; Kiwa, T. Small eddy current testing sensor probe using a tunneling magnetoresistance sensor to detect cracks in steel structures. *IEEE Trans. Magn.* **2018**, *54* (11), 1−5.

(23) Liu, L.; Yu, J.; González-Hernández, R.; Li, C.; Deng, J.; Lin, W.; Zhou, C.; Zhou, T.; Zhou, J.; Wang, H.; et al. Electrical switching of perpendicular magnetization in a single ferromagnetic layer. *Phys. Rev. B* **2020**, *101* (22), 220402.

(24) Tang, M.; Shen, K.; Xu, S.; Yang, H.; Hu, S.; Lü, W.; Li, C.; Li, M.; Yuan, Z.; Pennycook, S. J.; et al. Bulk Spin Torque-Driven Perpendicular Magnetization Switching in L10 FePt Single Layer. *Adv. Mater.* **2020**, *32* (31), 2002607.

(25) Liu, L.; Lee, O. J.; Gudmundsen, T. J.; Ralph, D. C.; Buhrman, R. A. Current-induced switching of perpendicularly magnetized magnetic layers using spin torque from the spin Hall effect. *Phys. Rev. Lett.* **2012**, *109* (9), 096602.

(26) Zhang, S.; Li, S.; Guo, Z.; Xu, Y.; Li, R.; Chen, Z.; Song, M.; Yang, X.; Li, L.; Zou, X.; et al. Nanoscale Vector Magnetic Sensing with Current-Driven Stochastic Nanomagnet. *Adv. Electron. Mater.* **2024**, *10*, 2300753.

(27) Jeng, J. T.; Chiang, C. Y.; Chang, C. H.; Lu, C. C. Vector magnetometer with dual-bridge GMR sensors. *IEEE Trans. Magn.* **2014**, *50* (1), 1−4.

(28) Dharmawan, I. D. M. O.; Lee, J.; Wang, D.; Kim, J. Measurement of three-dimensional distribution of magnetic flux density inside a grain of ferromagnetic materials: An experimental investigation. *Measurement* **2023**, *222*, 113695.

(29) Lu, C. C.; Huang, J. A 3-axis miniature magnetic sensor based on a planar fluxgate magnetometer with an orthogonal fluxguide. *Sensors* **2015**, *15* (6), 14727−14744.